International Journal of Nanomedicine

Dovepress
open access to scientific and medical research

Open Access Full Text Article

ORIGINAL RESEARCH

Indocyanine Green-Based Theranostic Nanoplatform for NIR Fluorescence Image-Guided Chemo/Photothermal Therapy of Cervical Cancer

Rong Ma,[1,*] Nuernisha Alifu,[2,*] Zhong Du,[1] Shuang Chen,[1] Youqiang Heng,[1] Jing Wang,[1] Lijun Zhu,[2] Cailing Ma,[1] Xueliang Zhang[2]

[1]State Key Laboratory of Pathogenesis, Prevention, and Treatment of High Incidence Diseases in Central Asia/ Department of Gynecology, The First Affiliated Hospital of Xinjiang Medical University, Urumqi, People's Republic of China; [2]State Key Laboratory of Pathogenesis, Prevention and Treatment of High Incidence Diseases in Central Asia School of Medical Engineering and Technology, Xinjiang Medical University, Urumqi, People's Republic of China

*These authors contributed equally to this work

Correspondence: Cailing Ma
State Key Laboratory of Pathogenesis, Prevention, and Treatment of High Incidence Diseases in Central Asia/Department of Gynecology, The First Affiliated Hospital of Xinjiang Medical University, Urumqi, 830054, People's Republic of China
Tel +86-13009661999
Email hymcl13009661999@126.com

Xueliang Zhang
State Key Laboratory of Pathogenesis, Prevention and Treatment of High Incidence Diseases in Central Asia, School of Medical Engineering and Technology, Xinjiang Medical University, Urumqi, 830011, People's Republic of China
Tel +86-18999978069
Email shuxue2456@126.com

Purpose: Indocyanine green (ICG) is a favorable fluorescence nanoprobe for its strong NIR-I fluorescence emission and good photothermal capabilities. However, the stability and tumor targeting ability of ICG is poor, which limits its further applications. To further improve the photothermal and therapeutic efficiency of ICG, bovine serum albumin (BSA) was utilized to encapsulate the ICG and the chemotherapeutic drug doxorubicin (DOX) was loaded to form the BSA@ICG-DOX theranostic nanoplatform.

Methods: In this study, ICG-loaded BSA nanoparticles (NPs) and the BSA@ICG-DOX NPs were fabricated using reprecipitation methods. Next, the tumour inhibition ability and biocompatibility of the NPs were evaluated. A subcutaneous xenografted nude mice model was established and imaging guided synergetic therapy was performed with the assistance of BSA@ICG-DOX NPs under 808 nm laser irradiation.

Results: The BSA@ICG NPs exhibited strong NIR-I fluorescence emission, excellent photothermal properties, biocompatibility, and tumor targeting ability. To further improve the therapeutic efficiency, the chemotherapeutic drug doxorubicin (DOX) was loaded into the BSA@ICG NPs to form the BSA@ICG-DOX theranostic nanoplatform. The BSA@ICG-DOX NPs were spherical with an average size of ~194.7 nm. The NPs had high encapsulation efficiency (DOX: 19.96% and ICG: 60.57%), and drug loading content (DOX: 0.95% and ICG: 3.03%). Next, excellent NIR-I fluorescence and low toxicity of the BSA@ICG-DOX NPs were verified. Targeted NIR-I fluorescence images were obtained after intravenous injection of the NPs into the subcutaneous cervical tumors of the mice.

Conclusion: To improve the anti-tumor efficiency of the ICG@BSA NPs, the chemotherapeutic drug DOX was loaded into the BSA@ICG NPs. The NIR excitation/emission and targeted BSA@ICG-DOX NPs enables high-performance diagnosis and chemo/photothermal therapy of subcutaneous cervical tumors, providing a promising approach for further biomedical applications.

Keywords: cervical cancer, indocyanine green, chemo/photothermal therapy, nanoparticles, near-infrared fluorescence imaging

Introduction

Cervical cancer is a common gynecological malignancy and is the primary cause of cancer-related death among females.[1–3] Although screening and the human papillomavirus (HPV) vaccine have helped reduce cervical cancer incidence rates, their applications are still not common practice for every patient.[4,5] The standard treatment for

Received: 7 May 2021
Accepted: 30 June 2021
Published: 17 July 2021

Graphical Abstract

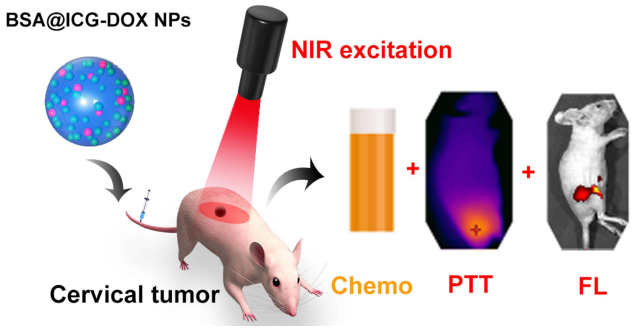

cervical cancer patients is palliative chemo, radio, and targeted therapies.[6,7] Although these therapeutic methods play an important role in treating cervical cancer, their side effects and drug resistance are still a challenge that needs to be overcome within clinical practice.[8,9] Among the traditional treatment methods, chemotherapy is useful in treating cervical cancer. Doxorubicin (DOX) is a clinically used chemotherapeutic drug, which has an inhibitory effect on a variety of tumors.[10,11] However, DOX-based chemotherapy still has low efficiency and a lack of specificity. Efforts have been made to solve this problem, and among them, targeted synergistic therapy is an attractive option. Photothermal therapy (PTT) is a noninvasive and efficient tumor treatment method.[12–15] PTT is based on a photothermal agent that converts light excitation energy into heat in order to induce tumor ablation. Combing PTT with chemotherapy makes full use of the advantages of both therapeutic methods and could help to achieve a higher treatment efficiency. Synergetic agents with targeting abilities play a vital role in the process of synergistic therapies.[16–19] In addition, diagnostic technologies with good imaging characteristics are in severe need.

Fluorescence imaging is a powerful method to study complex biological processes due to its high sensitivity and spatial resolution.[20–22] However, the traditional fluorescence imaging based on visible light (400–760 nm) still suffers from low contrast and high autofluorescence.[23,24] In comparison, the light in the near-infrared (NIR, 760–900 nm) spectral wavelength region has less scattering when traveling through biological samples/tissues.[25–27] Thus, NIR light can penetrate and excite deep-tissue regions under the skin. Moreover, NIR fluorescence imaging can offer high contrast and spatial resolution with high sensitivity with limited autofluorescence. Because of the NIR's fluorescent properties, effective tumor detection can be obtained via the NIR light excitation as well as the NIR light emission,[28,29] which have great potential in cervical cancer diagnosis.

Fluorescent nanoprobes that can simultaneously achieve targeted imaging, as well as synergistic therapy are very popular. Indocyanine green (ICG) is a NIR emissive fluorescent/photothermal agent approved by Food and Drug Administration (FDA).[30,31] Nevertheless, ICG has some disadvantages, such as limited photostability, a moderate fluorescence quantum yield, a high plasma protein binding rate, and undesired aggregation in aqueous solutions, limiting its applications in biomedical research.[32] ICG loaded albumin protein nanoparticles (NPs) are ideal choices with the advantages of biodegradability and high chemical stability, helping to solve the problems mentioned above. Albumin is a transporter of endogenous circulating proteins in the blood as well as various exogenous compounds in the vascular system. Serum albumin preferentially accumulates at the site of the tumor site giving it good natural tumor targeting capabilities.[33–35] Thus, albumin-based NPs provide the basis for tumor-based accumulation. Therefore, loading ICG into albumin to form NPs could construct an optimized nanoplatform that can significantly enhance tumor diagnosis.[36–38]

In this study, albumin-based NPs consisting of Bovine Serum Albumin (BSA) and ICG were developed. The ICG@BSA NPs showed good biocompatibility, low cytotoxicity, photothermal properties, and NIR fluorescence emission. Next, the ICG@BSA NPs were intravenously injected into the subcutaneous cervical tumor bearing nude mice. Further, good cervical tumor targeting abilities of ICG@BSA NPs were confirmed using an in vivo NIR

fluorescence imaging system. Moreover, to improve the anti-tumor efficiency of the ICG@BSA NPs, the chemotherapeutic drug DOX was loaded into the BSA@ICG NPs. Finally, in the subcutaneous cervical tumor mice, a high in vivo chemo/photothermal therapy efficiency was achieved.

Materials and Methods

Materials

Indocyanine green (ICG), doxorubicin hydrochloride (DOX ·HCl) and bovine serum albumin (BSA) [R-TE-156, CAS:3599–32-4; R-H-65212, CAS:25316–40-9; R-FB-001, Rui xi Biological Co. Ltd. Xi'an, China]. Ethanol (anhydrous) and dimethyl sulfoxide (DMSO) were purchased from Sigma-Aldrich. 4′,6-diamidino-2-phenylindole (DAPI) (C0065, Solarbio Science & Technology Co., Ltd. Beijing, China). Dulbecco's modified eagle medium (DMEM) cell culture medium and 1 × Phosphate Buffered Saline (PBS) buffer (PH=7.4) (B540626-0500, Sangon Biotech Co., Ltd. Shanghai, China). Deionized (DI) water was collected from a Milli-Q water purification system (Type 1, Millipore China Co., Ltd, New Jersey state, USA). All other chemicals and reagents were of analytical grade as purchased.

Preparation of BSA@ICG and BSA@ICG-DOX Nanoparticles

The method of preparing BSA@ICG was according to the previously reported reprecipitation method.[39] Briefly, ICG and BSA were dissolved in 20 mL DI water at ratios of 5%, 2%, 1%, 0.5%, 0.2%, and 0.1%. Next, ethanol (anhydrous) was added dropwise to the mixed solution to form aggregates under vigorous stirring. The mixture was stirred at 1000 rpm for 1 h in the dark at room temperature and then dialyzed in water (5 KD, 24 h) to remove any free ICG and ethanol. The contents of the ICG were increased to enhance the photothermal effects of the NPs. The ICG concentration was determined via UV-vis-NIR absorption spectra. Subsequently, the BSA@ICG NPs were collected in the supernatant after centrifugation at 8000 rpm for 10 min to remove the precipitate impurities.

The doxorubicin hydrochloride was desalted, and triethylamine was added after stirring overnight. Next, DOX was precipitated by centrifugation and dissolved in ethanol. Then, the dissolved albuprotein and the ICG were added to water and mixed, and then the DOX dissolved in ethanol that was be stirred for 30 min followed by centrifugation at 8000 rpm in an ultrafiltration tube to obtain the NPs. The newly formed and loaded NPs were then dialyzed overnight (MWCO of the dialysis bag was 5Kd). Finally, the BSA@ICG-DOX NPs were obtained and characterized the next day.

The molecular weight of ICG in our study is 775, so the M. wt of ICG is 775 g/mol. For every 10 milliliters of the system, BSA@ICG NPs: Albumin 50 mg, ICG2.034 mg, drug loading 4.07%, encapsulation rate 81.36%; BSA@ICG-DOX NPs: Albumin 50 mg, ICG 1.514 mg, DOX 0.48 mg, drug loading 3.03%, encapsulation rate 60.57%; DOX drug loading 0.95%, encapsulation rate 19.96%.

Characterization of the BSA@ICG and BSA@ICG-DOX NPs

To determine the drug loading content (DLC) and encapsulation efficiency (EE), supernatants from three cycles of centrifugations were collected when preparing the BSA@ICG-DOX NPs and the BSA@ICG NPs. The fluorescence and absorption spectra of collected supernatants after each wash step was measured using a Shimadzu UV-1800 spectrophotometer. The amount of ICG and DOX in the supernatants were determined according to the corresponding calibration curves (absorbance intensity vs concentration) at 488 nm and 780 nm, respectively. Then, the drug loading content (DLC) and encapsulation efficiency (EE) for both drugs were calculated according to formulas (1) and (2), respectively.

$$DLC = \frac{(W\text{Fed drug} - W\text{Drug in supernatant})}{W\text{Composite NPs}} \times 100\% \quad (1)$$

$$EE = \frac{(W\text{Fed drug} - W\text{Drug in supernatant})}{W\text{Fed drug}} \times 100\% \quad (2)$$

The morphology and structure of the BSA@ICG and BSA@ICG-DOX NPs were characterized by transmission electron microscope (TEM, FEI Tecnai G2 F20 S-Twin TEM, Hillsboro, OR). The dynamic diameter and distribution were characterized using dynamic light scattering (DLS) at 25 °C via a Zetasizer Nano-ZS90 (Malvern, UK). The absorption spectra were obtained from a LAMBDA 750 UV/Vis/NIR spectrophotometer (Perkin Elmer). The fluorescence emission spectra were measured with a fluorescence spectrometer (FluoroMax 4, Horiba Jobin-Yvon, Edison, NJ).

The photo-stability of the BSA@ICG and BSA@ICG-DOX NPs in the blood and acidic tumor environment was analyzed. Firstly, 50 μL of NPs was added into 500 μL of rat blood and acidic solutions (pH= 5.5, 6, 6.5, 7), then imaged under CLSM imaging system. Microscopic fluorescence images of the samples were obtained via a 10 × objective under 640 nm laser irradiation and 800–1000 nm wavelength detection. The change of fluorescence intensity of BSA@ICG and BSA@ICG-DOX NPs in the blood and acidic solutions (pH=5.5, 6, 6.5, 7) was monitored for 24 h and 48 h, respectively. The fluorescence intensity signals were acquired by Image J.

Cell Culture and Cytotoxicity Analysis

HeLa cells were purchase from Shanghai Genechem Co. Ltd. (The catalogue is GCC-UT 002RT). The cells were cultured in DMEM medium containing 10% fetal bovine serum, 1% (v/v) penicillin and 1% (v/v) streptomycin. The cells were incubated in a humidified incubator at 37 °C with 5% CO_2 atmosphere.

HeLa cells were seeded into 96-well plates at a cell density of 5×10^3 cells per well (200 μL cell culture medium) and cultured for 24 h (5% CO_2, 37°C). The cytotoxicity of BSA@ICG NPs and DOX/BSA was analyzed. HeLa cells were incubated with DOX/BSA alone respectively (concentration of DOX: 0 μg/mL, 2 μg/mL, 3.75 μg/mL, 6.25 μg/mL, 12.5 μg/mL, 25 μg/mL; concentration of BSA: 0 mg/mL, 0.2 mg/mL, 0.375 mg/mL, 0.625 mg/mL, 1.25 mg/mL, 2.5 mg/mL). In the meantime, the HeLa cells were incubated with BSA@ICG NPs at different concentrations (equivalent concentration of ICG at 0 μg/mL, 3.125 μg/mL, 6.25 μg/mL, 12.5 μg/mL, 25 μg/mL, 50 μg/mL) for 24 h. A standard Cell Counting Kit-8 assay (Dojindo) assay was employed to evaluate the HeLa cell viability.[40] After a 24 h treatment with BSA@ICG NPs and DOX/BSA at different concentrations, the cytoviability of the cells treated with 0 μg/mL BSA@ICG NPs and DOX/BSA alone was set as 1.0 and the cytoviability of the other wells was normalized to this reference value. The experiment was performed in triplicate at each concentration.

Confocal Laser Scanning Microscope (CLSM) Fluorescence Imaging of Cells

HeLa cells were seeded into a cell culture dish (35 mm in diameter) equipped with a glass bottom (0.13 mm in thickness) and incubated for 12 h. Equal amounts of culture medium containing BSA@ICG NPs, NPs (100 μg/mL of ICG) were added to the culture dish. After a 4 h incubation, the medium was discarded, and the cells were washed with 1 × PBS (pH=7.4) three times. Then, the cells were stained with DAPI for 10 min, and rinsed three times with 1 × PBS (pH=7.4). Cellular uptake and NIR fluorescence imaging were monitored via a confocal laser scanning microscope (CLSM) (Leica, TCS-SP5) using the DAPI and ICG observation channels whose maximum excitation/emission (E_x/E_m) wavelengths were 405/480 nm and 640/810 nm, respectively. Cell images were collected using static capture, microscopic images of the fixed samples were acquired using at a 60 × objective.

Animal

All animals utilized in this work were purchased from Beijing Vital River Laboratory Animal Technology Co, Ltd. The mice were housed in the specific pathogen free (SPF) barrier facilities of the Experimental Animal Center of Xinjiang Medical University. The animal room's ambient temperature and relative humidity are maintained at 22°C~ 26°C, and 40% ~ 60%, respectively. The chow and drinking water are treated aseptically, allowing ad libitum eating and drinking. All the experimental operations are satisfied under the Management of the Institution Animal Care and Use Committee of Xinjiang Medical University. All protocols were presented and approved for these studies. All animal procedures were performed in accordance with the National Institutes of Health Guide for the Care and Use of laboratory animals and were approved by the approval of the Animal Care and Usage Committee of Xinjiang Medical University (20191113–08).

Establishment of Cervical Tumor Model in vivo

Female BALB /c nude mice (4~6 weeks old) were subcutaneously injected with 1×10^7 /mL HeLa cells into the right hind leg of the mice. Tumors were allowed to grow for ~2 weeks. The animals body weight and tumor size were measured every other day. The tumor size was calculated according to the following formula: Volume = (length × width^2)/2. When the volume reached 50 mm^3, the HeLa cell-xenografted nude mice were grouped (n = 4 in each group) and treated with the different drug platforms.

Histology Analysis

Four groups (each group = 5 mice) of healthy female ICR mice were utilized. Two groups were intravenously injected with a BSA@ICG-DOX NPs solution at a dose of 10 mg/kg (counted by ICG concentration). The other two groups were injected with 1 × PBS. 24 h and 7 days post-injection the major organs (heart, lung, liver, spleen, and kidney) were harvested for hematoxylin-eosin staining (H&E). The H&E tissues were then examined using an inverted digital microscope (Leica). The control group received vehicle alone.

Ex vivo Photothermal Properties and Photothermal Conversion Efficiency of the Nanoparticles

The photothermal effects of BSA@ICG NPs were evaluated by detecting its temperature variation (200 μg/mL, counted by ICG concentration) under 808 nm laser irradiation (0.4 W/cm^2) for 10 min. The temperature was recorded every 30 s. An equal volume of DI water and free ICG with the same concentrations were used as blank and control, respectively. Infrared thermal imager was used to monitor the temperature rise curves for different agents under 808 nm laser, different power density, various BSA@ICG NPs concentrations, temperature variation of BSA@ICG NPs aqueous dispersion for 10 min. Furthermore, we monitored the temperature of BSA@ICG NPs dispersion (equivalent ICG concentration of 200 μg/mL) under 5 periods of laser irradiation on/off (10 min each period).

The photothermal conversion efficiency (η) of BSA@ICG NPs (concentration of ICG: 200 μg/mL) was measured as follows: BSA@ICG NPs were dispersed into the deionized water and irradiated under an 808 nm NIR laser excitation (0.4 W/cm^2, 10 min). The temperature curve during laser on and off was recorded, and the η could be calculated by the following equation:[41–43]

$$\eta = \frac{M_D C_D \left(T_{max} - T_{max,water}\right)}{\tau_s I \left(1 - 10^{-A_{808}}\right)} 100\% \quad (3)$$

T_{max} and $T_{max,water}$ are maximum equilibrium temperature for NPs solution and water, where I is the NIR laser power, and A_{808} stands for the absorbance of dispersion at 808 nm, by using the system time constant τ_s with the help of the mass (M_D) and the heat capacity (C_D) of deionized water.

In vivo Tumor-Targeting NIR Fluorescence Imaging

For in vivo NIR fluorescence imaging, aqueous solutions of ICG and BSA@ICG NPs (10 mg/kg, counted by ICG) were intravenously injected into HeLa cell tumor-bearing BALB/c mice via the tail vein when the tumor volume reached ~ 50 mm^3. The fluorescence signals of ICG were captured using a Maestro™ in vivo fluorescence imaging system (CRI Inc., USA) under a 745 nm laser excitation and emission filter that has a long pass of 840 nm. At 24 and 48 h post-injection, the mice were anesthetized with isoflurane and imaged. At 24 h post-injection, three mice were sacrificed, and the main organs (heart, liver, spleen, lung and kidney) and tumor were collected and imaged to evaluate the biodistribution of the BSA@ICG NPs.

In vivo Therapeutic Efficacy of BSA@ICG-DOX NPs

When the tumor size reached ~ 50 mm^3, HeLa tumor bearing mice were divided into four groups randomly (n = 4 in each group) as follows: BSA@ICG-DOX NPS group as BSA@I-D for short. (i) PBS for control group (ii) Laser group only (808 nm, 0.4 W/cm^2, 10 min), (iii) BSA@ICG-DOX group only (270 μL NPs added 30μL of PBS (10 ×) and (iv) BSA@ICG-DOX and laser (808 nm, 0.4 W/cm^2, 10 min). At 24 h post-intravenous injection, the tumor sites were irradiated with a NIR laser (808 nm, 0.4 W/cm^2) for 10 min. The laser beam was adjusted to cover the entire tumor region. The tumor volumes were measured every other day during the following 2 weeks. The changes in body weight were also recorded at the same time to evaluate the in vivo side effects of the therapy. Mice were sacrificed by cervical dislocation under anesthesia upon the completion of each experiment.

Statistical Analysis

Data are shown as mean ± SD. Three independent experiments were conducted with three replicates (n = 3). For statistical analysis, a Mann−Whitney-*U*-test was performed using Origin 9.1 software (OriginLab, Northampton, USA). Image J software was used to analyze the fluorescence images. A student' s tests were used to compare the intensities. Values of $P < 0.05$ were considered significant.

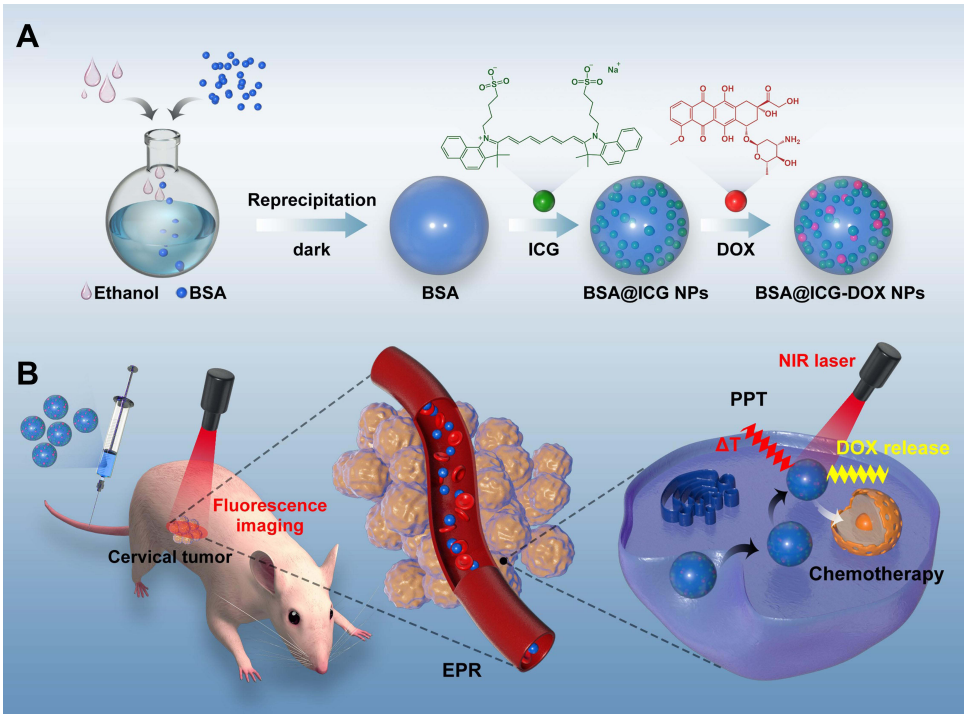

Scheme 1 Schematic illustration of BSA@ICG-DOX NPs for NIR fluorescence image-guided chemo/photothermal therapy of cervical cancer. (**A**) The preparation of BSA@ICG NPs and BSA@ICG-DOX NPs; (**B**) BSA@ICG-DOX NPs tissue accumulation elevates anti-tumor activities.

Results

Preparation and Characterization of BSA@ICG and BSA@ICG-DOX NPs

The synthesis procedure of BSA@ICG NPs and BSA@ICG -DOX NPs were illustrated in Scheme 1. Free ICG and BSA were first dispersed in water and ethanol was added to the mixture. Via hydrogen bonds and hydrophobic interactions, the solubility of albumin was reduced to further form the BSA@ICG NPs. The BSA@ICG NPs act as a protective carrier to minimize the removal of ICG molecules from either the circulatory system or being recognized and degraded by the reticular endothelial system (RES). Thus, the stability and fluorescence of the loaded ICG were maintained. The drug loading content (DLC) and encapsulation efficiency (EE) of BSA@ICG NPs and BSA@ICG-DOX NPs were demonstrated via absorption spectra. The EE for DOX and ICG was calculated as 19.96% and 60.57%, and the DLC for DOX and ICG were determined at 0.95% and 3.03%, respectively.

After synthesis and drug loading, the BSA@ICG NPs and BSA@ICG-DOX NPs in an aqueous dispersion were characterized. As shown in Figure 1A, ICG in an aqueous solution had an absorption peak at 787 nm (black line). After loading into BSA (BSA@ICG NPs), the absorption peak red-shifted to 801 nm. The loading of DOX also red-shifted the absorption peak to 809 nm. Moreover, the fluorescence spectra of ICG and the ICG-loaded NPs were measured. As shown in Figure 1B, BSA@ICG NPs in an aqueous solution had a fluorescence peak at 836.8 nm, the loading of DOX red-shifted the peak after being loaded into BSA (BSA@ICG-DOX NPs), the absorption fluorescence peak red-shifted to 837.2 nm. The fluorescence of the BSA@ICG NPs in an aqueous solution was significantly stronger than that of the free ICG solution. In contrast, the BSA@ICG-DOX NPs solution showed decreased fluorescence at the same ICG concentration. Both the absorption and fluorescence peaks of BSA@ICG-DOX NPs located at the NIR spectral wavelength region are ideal for in vivo fluorescence imaging with less scattering and low autofluorescence.

The morphology and size of the NPs were confirmed using TEM and DLS methods. As shown in Figure 1C, BSA@ICG NPs and BSA@ICG-DOX NPs exhibited a similarly uniform spherical structure with an average diameter of 159.3 nm and 194.7 nm, respectively. The polydispersity index (PDI) of BSA@ICG NPs was found to be 0.076, and BSA@ICG NPs was 0.055, respectively. The size obtained from the TEM images (inset of

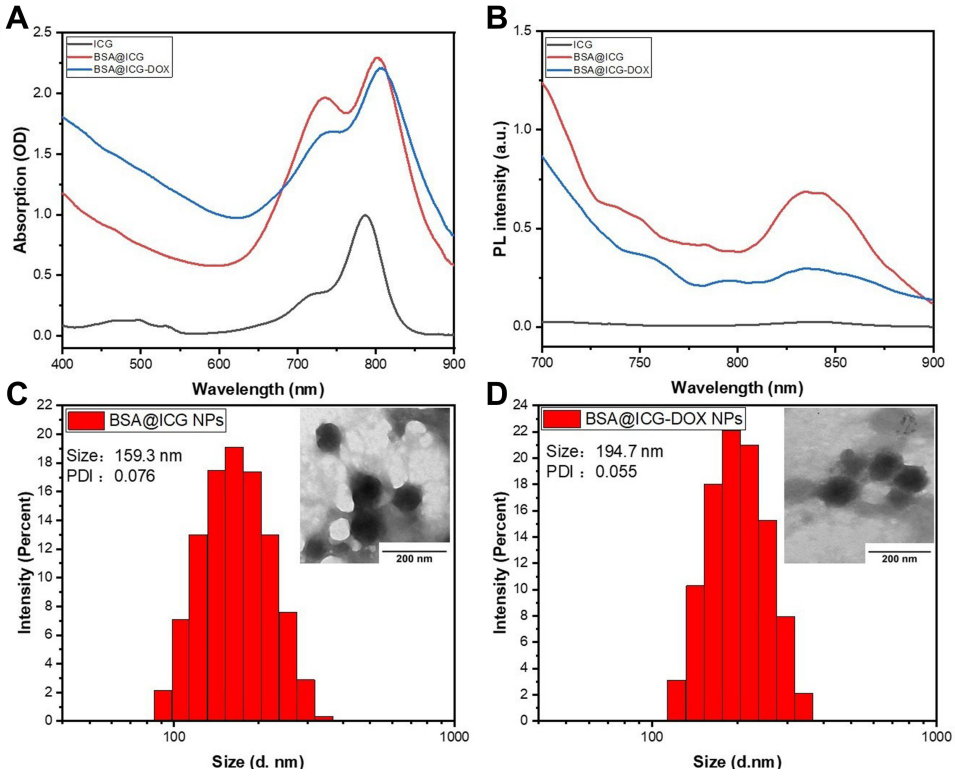

Figure 1 Characterization of BSA@ICG NPs and BSA@ICG-DOX NPs in an aqueous dispersion. (**A**) Absorption spectra of free ICG (200 μg/mL), BSA@ICG NPs (200 μg/mL) and BSA@ICG-DOX NPs (150 μg/mL) in an aqueous dispersion; (**B**) Fluorescence spectra of free ICG, BSA@ICG NPs and BSA@ICG-DOX NPs in an aqueous dispersion. (**C**) and (**D**) DLS and polydispersity index (PDI) results of BSA@ICG NPs and BSA@ICG-DOX NPs. Inset: Representative TEM images of BSA@ICG NPs and BSA@ICG-DOX NPs. A theranostic nanocomplex that is self-assembled from ICG and BSA is prepared and optimized for enhanced tumor imaging and excellent hydrolytic stability.

Figure 1C and D) matched well with the DLS characterization (Figure 1C and D). Therefore, the size of the obtained BSA@ICG NPs are suitable for in vivo tumor targeting.

The fluorescence stability of the BSA@ICG and BSA@ICG-DOX NPs in the blood and acidic solutions (pH=5.5, 6, 6.5, 7) was analyzed under a confocal microscope at 24 h and 48 h, respectively (Figure S1A and S1B). The fluorescence intensity of both BSA@ICG and BSA@ICG-DOX (BSA@I-D) NPs was maintained well (decreased less than 10%) as shown in Figure S1C–F. Furthermore, the fluorescence intensity of BSA@ICG and BSA@ICG-DOX NPs was increased with time. These results illustrated that the nanoparticles are very suitable in vivo environment and fluorescence imaging.

In vitro Photothermal Analysis

In this study various groups (free ICG, DOX, BSA, BSA@ICG NPs) were used to test the performance of the in vitro photothermal system (Figure 2B) in order to evaluate the photothermal properties of the BSA@ICG NPs (as demonstrated in Figure 2A). In group 1, the temperature change of various agents (equivalent concentration of ICG at 200 μg/mL) under 808 nm laser irradiation (0.4 W/cm^2) for 10 min were recorded under the same experimental conditions. The temperature of BSA@ICG NPs in an aqueous dispersion increased quickly to a high temperature of 51.2 °C (Figure 2B and E). The free ICG in an aqueous solution increased quickly, but the maximum temperature achieved was lower than that of the BSA@ICG NPs (Figure 2B and E). The temperature of DOX and BSA changed little under the same irradiation conditions (Figure 2B). Moreover, the temperature evaluation was proportional to the concentration of the BSA@ICG NPs (Figure 2C) and the excitation power density. (Figure 2D).

Next, the photothermal stability of the BSA@ICG NPs was further evaluated using a 5-cycle heating and cooling process. The 808 nm laser (0.4 W/cm^2) irradiated the aqueous dispersion of BSA@ICG NPs (equivalent concentration of ICG at 200 μg/mL) for 10 min in order to increase the temperature, then the irradiation was

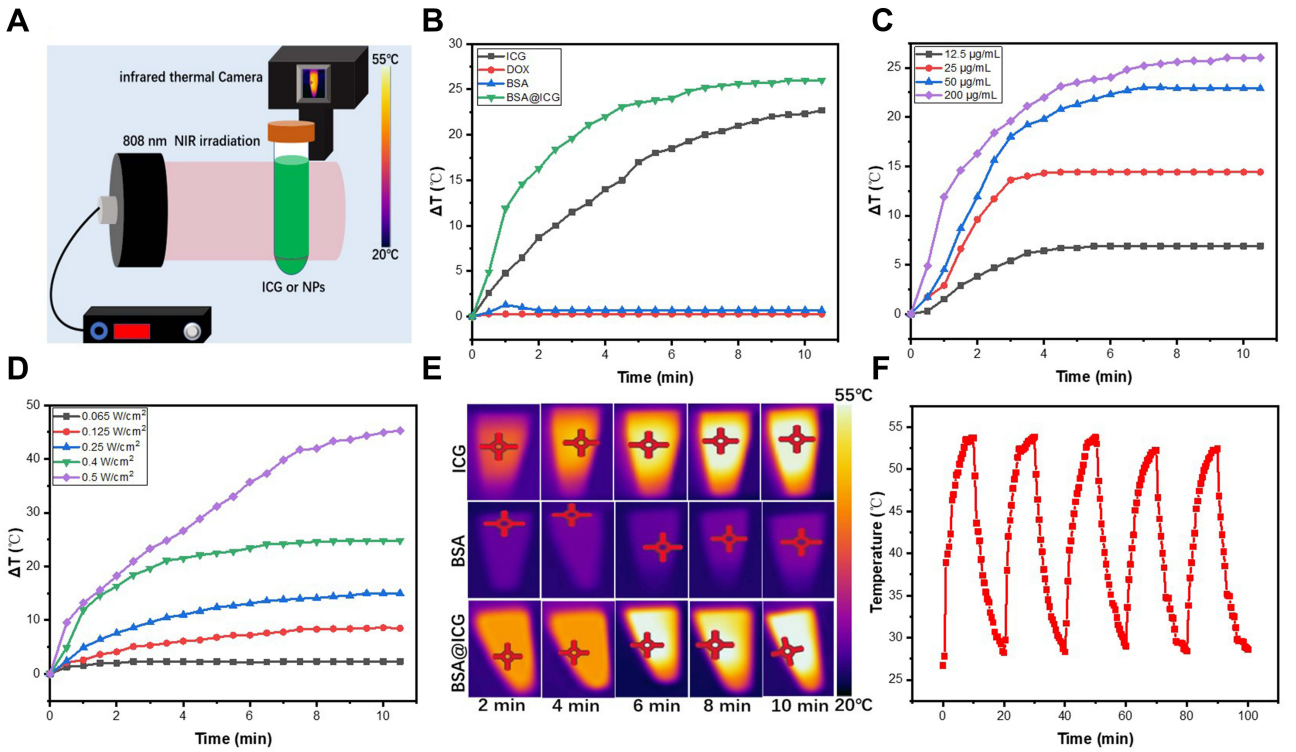

Figure 2 Photothermal properties of BSA@ICG NPs. (**A**) Schematic illustration of in vitro photothermal experimental system; (**B**) Temperature elevation curves of various agents (free ICG, DOX, BSA, BSA@ICG NPs) (equivalent concentration of ICG at 200 μg/mL) under NIR laser irradiation for 10 min; (**C**) Temperature elevation of BSA@ICG NPs at various concentrations under NIR laser irradiation; (**D**) Temperature elevation of BSA@ICG NPs (200 μg/mL) under NIR laser irradiation with different power density; (**E**) Infrared thermal images of ICG, BSA, and BSA@ICG NPs in an aqueous dispersion under NIR laser irradiation; (**F**) Temperature evaluation of BSA@ICG NPs (concentration of ICG:200 μg/mL) in aqueous dispersion under 5 irradiation/cooling cycles; Excitation: 808 nm, Power density: 0.4 W/cm^2.

removed. The BSA@ICG NPs in an aqueous dispersion naturally cooled to room temperature in 10 min. Fortunately, as shown in Figure 2F, under repetitive NIR irradiations, the BSA@ICG NPs dispersion showed photostability with only a 2.79% decrease in the peak temperature after five irradiation cycles. We calculated the photothermal conversion efficiency using the formula.[41,44] The η value of BSA@ICG NPs was measured and calculated to be 31.2% (Figure S2). The η value of ICG@BSA NPs is comparable to other ICG encapsulated polymeric nanoparticles, such as mPEG-ACA-ICG (20.81%)[43] and ICG-CD (30.25%).[42] Thus, the BSA@ICG NPs possessed NIR-I fluorescence properties as well as a photothermal effect and could serve as a theranostic fluorescence nanoprobe for cancer therapeutics.

Cellular Uptake

As shown in Figure S3, negligible cytotoxicity was observed in the BSA group even at a concentration as high as 5 mg/mL. This is due to its noninvasiveness, high biocompatibility, and ease of reversible application. As shown in Figure 3A, negligible cytotoxicity was observed even at a concentration as high as 50 μg/mL (counted by ICG concentration), indicating that the as prepared BSA@ICG NPs are highly biocompatible and safe for in vitro fluorescence imaging. The low cytotoxicity of BSA@ICG NPs could be ascribed to the intrinsic biocompatibility of ICG and BSA. Furthermore, the cells treated with the same concentration of free DOX drug (25 μg/mL) still survived at a rate of 50%. (Figure 3B). Next, the confocal laser scanning microscope (CLSM) imaging of NPs incubated with the HeLa cells was conducted. First, the HeLa cell nucleus was stained with DAPI (blue color) and then further stained with the NPs. After the HeLa cells were double stained, confocal fluorescence images of the cells were acquired using CLSM in both the blue (DAPI, E_x= 405 nm) and the red channel's (NPs, E_x= 640 nm), as shown in Figure 3C. Strong blue and red fluorescence emissions were observed from the blue and red channels of the HeLa cells. Both the free ICG, BSA@ICG and BSA@ICG-DOX NPs could label HeLa cells better with strong fluorescence emission. Cell uptake is an important factor that ultimately affects the

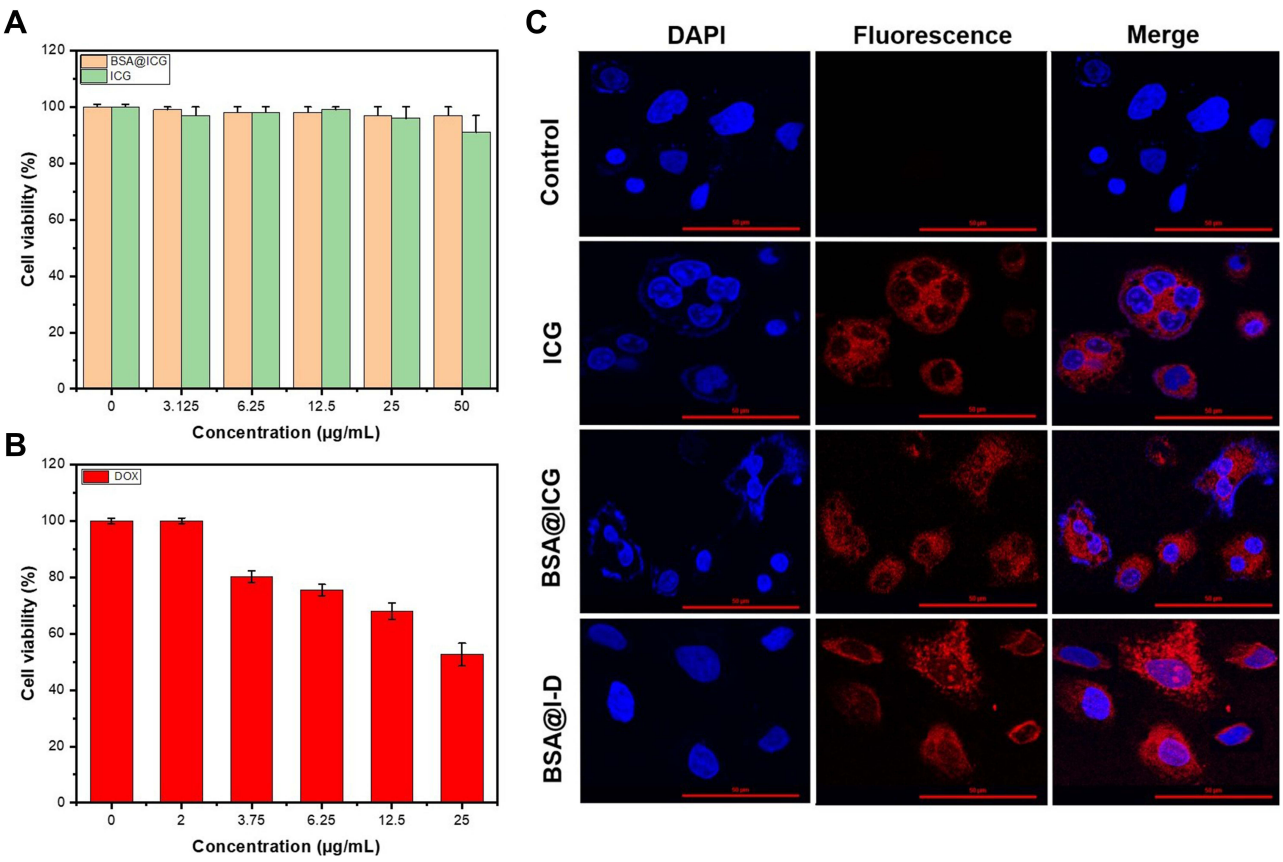

Figure 3 Cellular uptake analysis. (**A**) Cytoviability of Hela cells after incubation with BSA@ICG NPs at different concentrations for 24 h. Data are expressed as mean ± S. D. (n = 6 in each concentration) (**B**) Cytoviability of Hela cells after incubation with DOX at different concentrations for 24 h. Data are expressed as mean ± S.D. (n = 6 in each concentration) (**C**) Confocal scanning laser microscopic (CSLM) images of Hela cells incubated with free ICG, BSA@ICG NPs, and BSA@ICG-DOX (equivalent ICG concentration: 100 μg/mL) for 4 h (scale bars: 50 μm); the excitation for DAPI and ICG were 405 nm and 640 nm, respectively.

therapeutic efficacy of chemotherapy.[45,46] The cell uptaking way of our NPs is intracellular accumulation. These results demonstrated the biocompatibility and cellular uptake ability of the BSA@ICG and BSA@ICG-DOX NPs by HeLa cells.

In vivo NIR Fluorescence Imaging of BSA@ICG NPs

NIR fluorescence intensities of ICG, BSA@ICG NPs, and BSA@ICG-DOX NPs were compared at the same concentration of free ICG. As shown in Figure 4A, the NIR fluorescence intensity of BSA@ICG NPS was enhanced compared with free ICG. BSA@ICG-DOX NPs also emitted a relatively strong NIR fluorescence emission. Further, BSA@ICG NPS were intravenously injected into the tumor-bearing nude mice (Figure S4) and imaged under a NIR fluorescence imaging system. NIR fluorescence emissions from the tumor site were monitored. As shown in Figures 4B and S5, 24 h post-injection, NIR fluorescence intensity is observed from the tumor site reaching its maximum intensity and gradually decreasing at 48 h. Furthermore, the major organs (liver, lung, spleen, kidney, heart, and tumor) were excised at 48 h post injection and imaged under a NIR fluorescence imaging system. Strong NIR fluorescence emissions from the excised tumors and liver were observed, while the control group treated with PBS, had no fluorescence signal detection. These results confirm the tumor targeting ability as well as NIR fluorescence properties of BSA@ICG NPs in vivo.

In vivo Anti-Tumor Efficacy

Twenty mice with a tumor volume of 50 mm^3 were selected for in vivo PTT in order to evaluate the photothermal properties of BSA@ICG-DOX nanoparticles in HeLa cell tumor-bearing nude mice. To evaluate the in vivo photothermal and chemotherapeutic abilities of the NPs, 30 μL PBS (10 ×) and 270 μL BSA@ICG-DOX NPs were first

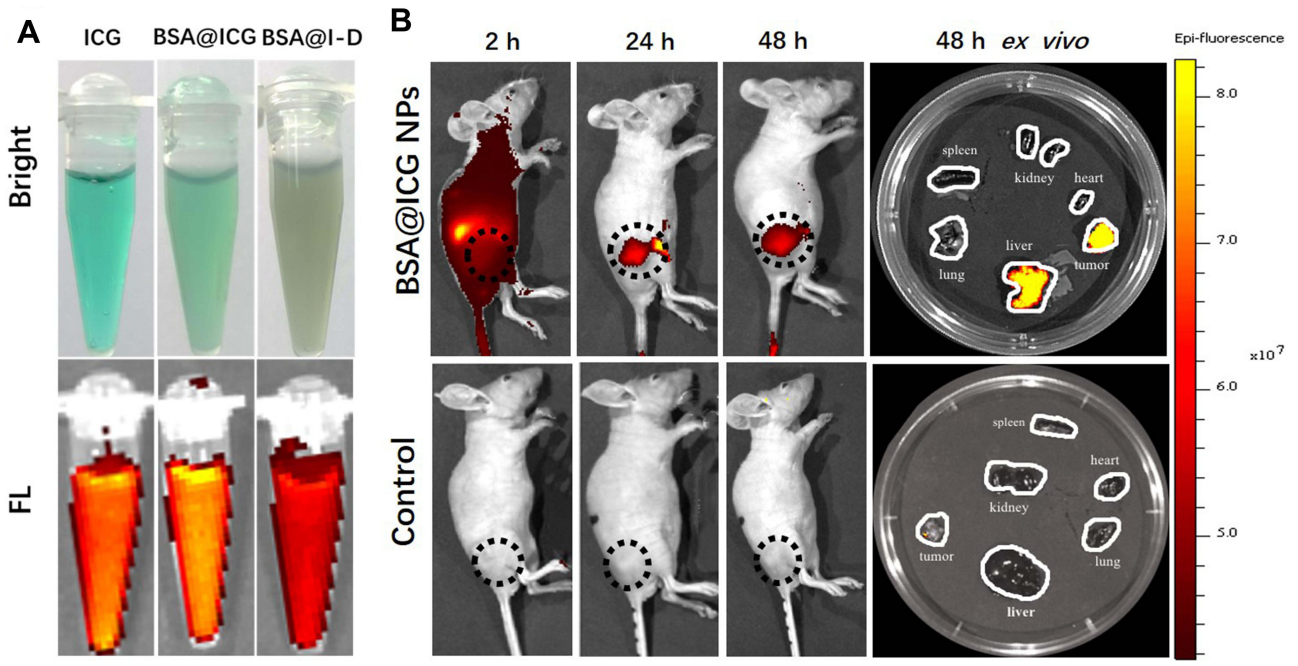

Figure 4 NIR fluorescence images of BSA@ICG NPs (**A**) Bright-field (BF) and NIR fluorescence (FL) images of ICG, BSA@ICG NPs, BSA@ICG-DOX NPs (BSA@I-D) (equivalent concentration of ICG at 200 μg/mL) under the in vivo NIR fluorescence imaging system; (**B**) NIR fluorescence images of BSA@ICG NPs injected tumor-bearing nude mice (black dotted circles are subcutaneous tumor site) and major organs at 48 h post injection. E_x: 745 nm, E_m: 840 nm.

intravenously injected into the tumor-bearing nude mice. These mice were randomly divided into four groups (n = 4 per group) as follows: (1) BSA@ICG-DOX NPs + Laser; (2) BSA@ICG-DOX NPs only; (3) Laser only; (4) Control. After a 10 min irradiation (808 nm, 0.4 W/cm^2), the temperature at the tumor site of the mice treated with the NPs quickly increased to 46°C, while the temperature of the control mouse only increased to 34°C as shown in Figure 5A and B. The high temperatures achieved in the NPs treated mice were sufficient destroy the tumor cells effectively. Next, we conducted the NPs assisted photothermal treatment of the subcutaneous cervical tumors in vivo. Cervical-tumor-bearing mice with approximately the same tumor volume were randomly divided into four groups (four mice in each group). The experimental group referred to the mice treated with both NPs and 808 nm laser irradiation (0.4 W/cm^2 for 10 min, 24 h post-injection) guided by the NIR-I fluorescence imaging. Three control groups included the mice treated with PBS alone, the mice treated with both PBS and 808 nm laser irradiation (0.4 W/cm^2 for 10 min, 24 h post-injection), and the mice treated with NPs alone. The growth rate of the tumors up to 15 days was monitored to evaluate the photothermal and chemotherapy ablation effects (Figure 5C). The tumors growth in the experimental group were inhibited during the 15-day observation period, as shown in Figure 5D, E, and Figure S6 respectively. Tumor-bearing nude mice with dashed circles in the bright field images after various treatments (Figure 5C), images of treated mice and their corresponding tumors excised at 14th day (Figure 5D), and variations of relative tumor volume and tumor weight in vivo at 2 weeks after various treatments (Figures 5E and S6. This data reveals that the BSA@ICG-DOX NPs had an excellent photothermal and chemotherapeutic effect. In contrast, the size of the tumors in the control groups showed sustained growth increases (Figure 5E), indicating that BSA@ICG-DOX NPs or laser irradiation alone could not inhibit tumor growth. The above results show that BSA@ICG-DOX NPs can act as an effective photothermal and chemotherapeutic theranostic agent to treat cervical cancer.

In vivo Biosafety

Biosafety is a critical factor in the development and translation of therapeutic nanoagents for biomedical applications. The in vivo toxicity of the NPs was further evaluated in mice via a histology study. As shown in Figure 6, the microscopic images of the H&E-stained tissues revealed that no noticeable short-term (24 h post-injection) and long-term (7 days post-injection) damage or inflammatory lesions could be observed in all the major organs (heart, liver, spleen, lung, and kidney) of the mice. Our results illustrated that the

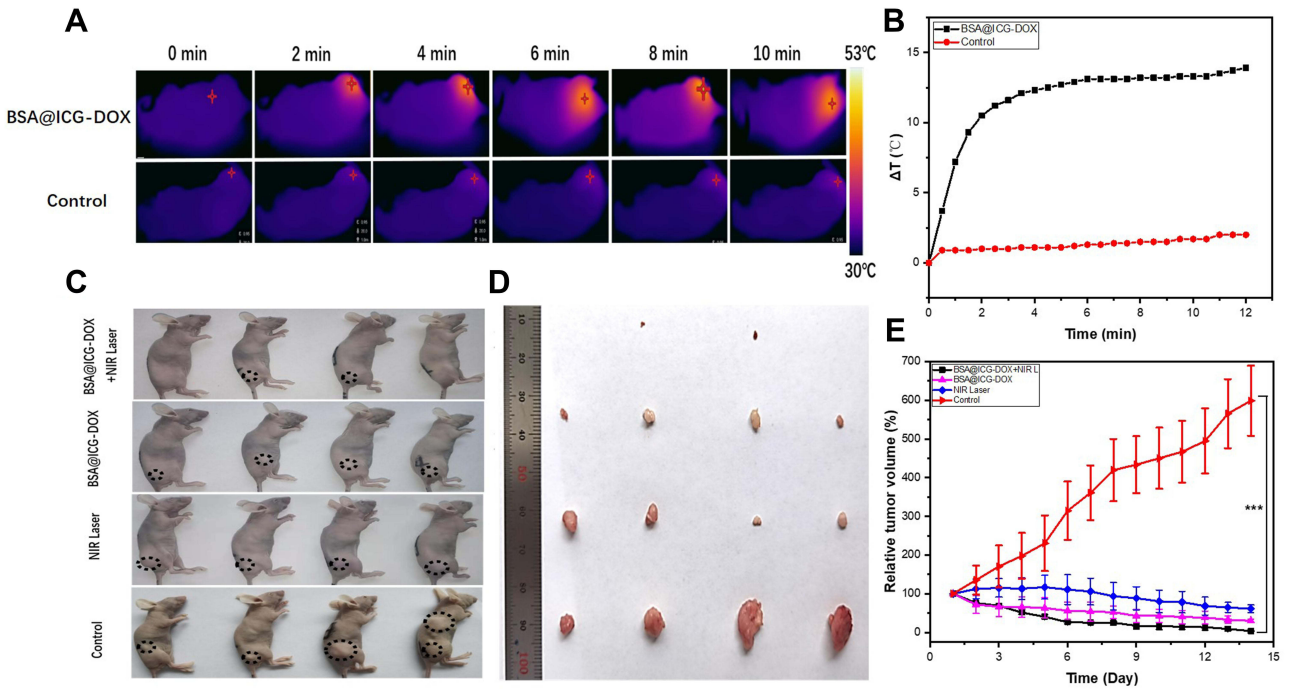

Figure 5 Evaluation of in vivo antitumor efficiency. (**A**) Infrared thermographic images of the HeLa cell tumor-bearing mice after NIR irradiation (808 nm, 0.4 W/cm^2, 10 min). (**B**) The corresponding temperature elevation curves for Figure 5A; (**C**) Tumor-bearing nude mice with dashed circles in the bright field images after various treatments and (**D**) Images of treated mice and their corresponding tumors excised at the 14th day.; (**E**) Variation of relative tumor volumes in vivo 2 weeks after various treatments; Data were displayed as the mean ± SD (n =4, ***p < 0.001 between two groups).

BSA@ICG-DOX NPs possessed good biocompatibility and are safe and non-toxic for in vivo theranostic applications.

Discussion

It is essential to utilize improved imaging and therapeutic modalities to achieve highly efficient and precise diagnosis and therapy. In vivo NIR fluorescence imaging has the advantages of minimal light scattering and decreased tissue autofluorescence, thus giving NIR agents a large penetration depth and improved spatial resolution. Combining NIR fluorescence with effective chemotherapeutic treatments in order to increase the efficacy of an image guided synergetic therapy is of great use for future clinical applications.[47,48] Theranostic nanoplatforms with good biocompatibility, NIR excitable/emissive, and favorable biosafety play a vital role in the field of NIR imaging-guided synergetic therapies.

ICG is an ideal photothermal agent as well as a NIR excitable/emissive (absorption peak at ~780 nm and emission peak ~810 nm) contrast agent that is approved by FDA. However, the photostability and tumor targeting ability of ICG is very poor. Thus, the application of ICG in biomedical applications is restricted. One way to solve this problem is to encapsulate ICG molecules into nanoparticles. One of the best nanodrug candidates is serum albumin. Albumin has been studied and widely used in the field of biomedical science for decades. The ICG loaded albumin protein theranostic nanoplatform can improve the photostability and tumor targeting ability of ICG while also maintaining its photothermal properties. To improve the efficiency of the treatment of cervical cancer, chemotherapy and PTT were combined. However, it is still a challenge to develop a multifunctional theranostic nanoplatform with both high brightness intensity and NIR excitation/emission as well as PTT and chemotherapeutic properties.

In this study, an albumin-based nanoparticle consisting of BSA and ICG was developed as a PTT and NIR excitable/emissive fluorescence agent (fluorescence emission peak at 809 nm and absorption peak at 808nm) for the treatment of cervical cancer. These BSA@ICG NPs were fabricated by the reprecipitation method. Further, the BSA@ICG NPs showed good biocompatibility, low cytotoxicity, and photothermal properties which were studied in vivo using NIR fluorescence imaging. The prepared BSA@ICG NPs were intravenously injected into cervical tumor-bearing mice via a tail vein injection. 24 h post-injection, deep-tissue and high-resolution NIR fluorescence imaging were conducted, revealing the effective targeting ability of the BSA@ICG NPs. Targeted

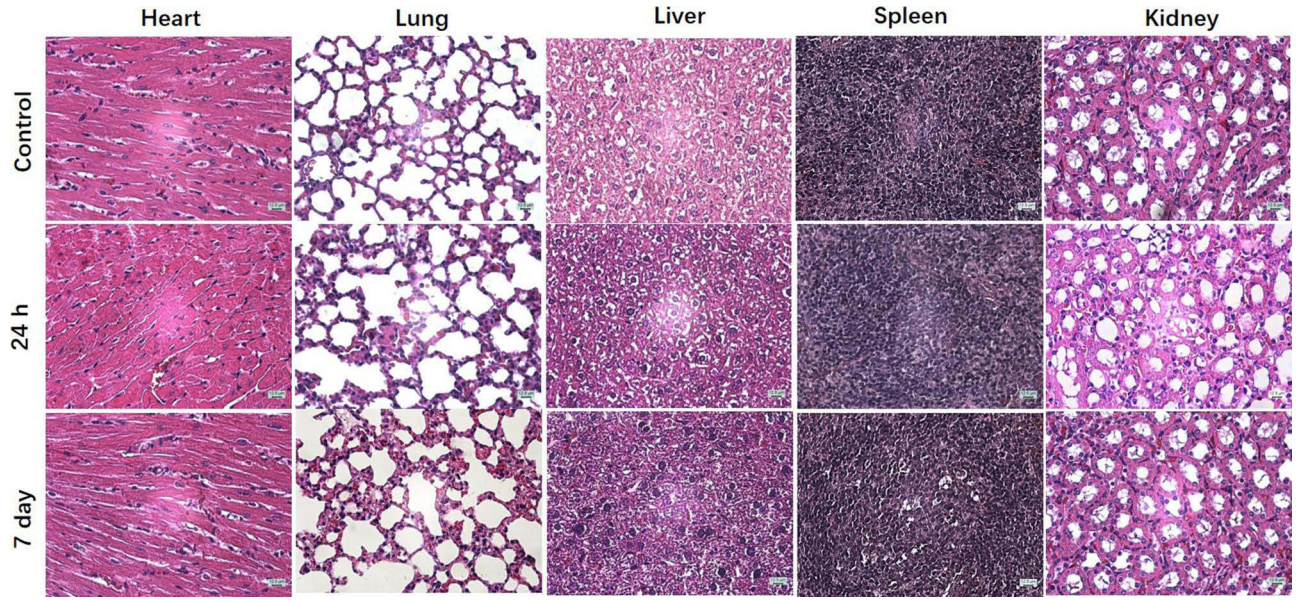

Figure 6 Histological analysis of major organs (heart, liver, spleen, lung, and kidney). BSA@ICG-DOX NPs from treated mice 24 h after intravenous injection and at day 7 post-injection (counted by ICG concentration). Scale Bar = 12.5 μm.

image-guided synergetic therapy is a very popular treatment method and is essential in improving anti-cancer therapeutic effects. The combination of PTT with chemotherapy has a significant potential for a better synergistic therapeutic effect.[49,50] DOX is an anti-tumor antibiotic, which has a broad inhibitory effect on tumors. When combined, ICG and DOX form discreet and homogenous nanoparticles. It is believed that the high temperature created by the excitation of ICG could stimulate the release of DOX.[51,52] Interestingly, albumin has two binding sites, and has the potential to load small molecules. In this study, we have exploited these binding pockets to load both ICG and DOX.

In this nano-system, the physical interactions of ICG, albumin, and DOX were enhanced using a high-pressure homogenization process. As a result, the absorption peak of the supernatants decreased compared with those of free drugs, which suggests successful drug (DOX or ICG) loading into the NPs. The encapsulation efficiency (EE) for DOX and ICG were calculated at 19.96% and 60.57%, and the drug loading content (DLC) for DOX and ICG were determined as 0.95% and 3.03%, respectively.

BSA@ICG NPs and BSA@ICG-DOX NPs exhibited a similar uniformly spherical morphology. The average diameter of BSA@ICG NPs was found to be 159.3 nm and BSA@ICG@DOX NPs was 194.7 nm. In general, a size less than 200 nm is considered to be ideal for the EPR effect. Further, co-encapsulating ICG and the anticancer drug DOX in BSA was optimized at a reasonable dose (concentration of ICG 150 μg/mL, DOX 50 μg/mL).

Using in vitro and in vivo NIR fluorescence imaging, the high biocompatibility and biosafety of BSA@ICG-DOX NPs were confirmed. The in vivo antitumor abilities of BSA@ICG-DOX NPs in a subcutaneous cervical tumor mouse model were evaluated. The BSA@ICG-DOX NPs were intravenously injected into tumor-bearing mice and thermal imaging was conducted 24 h of post-injection after treatment with a 808 nm laser. The temperature of the tumor site reached ~46 °C within 10 min, which was significantly higher than the control mice treated with PBS. Then the 808 nm excited chemo/photothermal therapy was conducted on tumors in nude mice treated with BSA@ICG-DOX NPs. The tumor volume and the weight of tumor-bearing mice were monitored for 2 weeks. The tumors in the experimental group treated with BSA@ICG-DOX NPs under 808 nm laser irradiation were significantly inhibited, revealing that the BSA@ICG-DOX NPs had excellent photothermal and chemotherapeutic effects. In comparison, the volume of the tumors in the control groups continuously increased, indicating that the tumor growth was not inhibited by NPs injection or laser irradiation alone. The results showed dissimilar trends of tumor growth over time after implementing different therapeutics. Specifically, single-modal Laser (single- NIR irradiation) therapeutics did not completely suppress tumor

growth. In the single-BSA@ICG-DOX NPs treated group, there was no significant tumor suppression effect in the absence of NIR irradiation compared with the control group treated with saline. However, in the experimental group injected with the combined nanotherapeutic platform BSA@ICG-DOX NPs showed a significant tumor inhibition effect, two mice showed complete tumor ablation. Moreover, the therapeutic agents did not cause any significant loss of mouse body weight during the entirety of the treatment process (Figure S7), indicating very low systemic toxicity under the applied dosages. The animal studies confirmed the strong combinatorial therapeutic efficacy of BSA@ICG-DOX NP mediated PTT/chemotherapy against cervical tumors in vivo. Additionally, the major organs of the treated mice were excised for histopathological analysis via H&E staining at 24 h and 7-day post injection further demonstrating the in vivo biosafety of the BSA@ICG-DOX NPs. Thus, the developed NIR excitable/emissive BSA@ICG-DOX NPs with good biocompatibility, biosafety, and high tumor inhibition efficiency have great potential in future clinical applications.

Conclusion

In summary, we developed an ICG based theranostic nanoplatform BSA@ICG-DOX NPs for NIR targeted imaging and photothermal/chemo dual therapy of cervical tumors in living mice. The modified ICG-based NPs show strong NIR emission, good biocompatibility and photothermal ability. In this work, a novel type of multifunctional theranostic nanoplatform BSA@ICG-DOX NPs were designed and synthesized. The BSA@ICG-DOX NPs showed strong NIR fluorescence emission and cervical tumour targeting ability, favorable photothermal property, good biocompatibility and low toxicity. Further, the BSA@ICG-DOX NPs were utilized for in vivo NIR fluorescence imaging-guided chemo/photothermal therapy of cervical tumour under 808 nm-laser irradiation. This study has shown the anticancer property of BSA@ICG-DOX NPs on cervical cancer. The NIR excitable/emissive and targeting BSA@ICG-DOX NPs enables well-performance diagnosis and chemo/photothermal therapy of subcutaneous cervical tumours, which provides a promising approach for further biomedical applications.

Acknowledgments

Hongli Wang, Yan Li and Li Zhang are grateful to the whole experiment application. Fundamental Research Funds for the Central Universities and State Key Laboratory of Pathogenesis, Prevention and Treatment of High Incidence Diseases in Central Asia Fund (SKL-HIDCA-2019-5, SKL-HIDCA-2019-3, SKL-HIDCA-2020-6), Xinjiang Autonomous Region Health Commission, Young Scientific and Technological Talents Project (WJWJ202012), Xinjiang Autonomous Region Collaborative Innovation Program (2019E0282). The First Affiliated Hospital of Xinjiang Medical University, Graduate Student Innovation Program of the Hospital (33-0104006). National Natural Science Foundation of China (82060326).

Disclosure

The authors report no conflicts of interest in this work.

References

1. Fitzmaurice C, Abate D, Abbasi N, et al. Global, Regional, and National Cancer Incidence, Mortality, Years of Life Lost, Years Lived With Disability, and Disability-Adjusted Life-Years for 29 Cancer Groups, 1990 to 2017: a Systematic Analysis for the Global Burden of Disease Study. *JAMA Oncol*. 2019;5(12):1749–1768. doi:10.1001/jamaoncol.2019.2996
2. Torre LA, Bray F, Siegel RL, et al. Global cancer statistics, 2012. *CA Cancer J Clin*. 2015;65(2):87–108. doi:10.3322/caac.21262
3. Vu M, Yu J, Awolude OA, et al. Cervical cancer worldwide. *Curr Probl Cancer*. 2018;42(5):457–465. doi:10.1016/j.currproblcancer.2018.06.003
4. Wang J, Tang D, Wang J, et al. Genotype distribution and prevalence of human papillomavirus among women with cervical cytological abnormalities in Xinjiang, China. *Hum Vaccin Immunother*. 2019;15(7–8):1889–1896. doi:10.1080/21645515.2019.1578598
5. Henley S, Thomas C, Lewis D, et al. Annual report to the nation on the status of cancer, part II: progress toward Healthy People 2020 objectives for 4 common cancers. *Cancer*. 2020;126(10):2250–2266. doi:10.1002/cncr.32801
6. Beaver J, Coleman R, Arend R, et al. Advancing Drug Development in Gynecologic Malignancies. *Clin Cancer Res*. 2019;25(16):4874–4880. doi:10.1158/1078-0432.Ccr-19-0619
7. Kim M, Suh D, Lee K, et al. Major clinical research advances in gynecologic cancer in 2019. *J Gynecol Oncol*. 2020;31(3):e48. doi:10.3802/jgo.2020.31.e48
8. Mazeron R, Gouy S, Chargari C, et al. Post radiation hysterectomy in locally advanced cervical cancer: outcomes and dosimetric impact. *Radiother Oncol*. 2016;120(3):460–466. doi:10.1016/j.radonc.2016.07.010
9. Spampinato S, Fokdal L, Pötter R, et al. Risk factors and dose-effects for bladder fistula, bleeding and cystitis after radiotherapy with imaged-guided adaptive brachytherapy for cervical cancer: an EMBRACE analysis. *Radiother Oncol*. 2021;158(3):312–320. doi:10.1016/j.radonc.2021.01.019
10. Liu B, Zhang X, Li C, et al. Magnetically targeted delivery of DOX loaded Cu9S5@mSiO2@Fe3O4-PEG nanocomposites for combined MR imaging and chemo/photothermal synergistic therapy. *Nanoscale*. 2016;8(25):12560–12569. doi:10.1039/c5nr06322a
11. Liu C, Guo Y, Hong Q, et al. Bovine Serum Albumin Adsorption in Mesoporous Titanium Dioxide: pore Size and Pore Chemistry Effect. *Langmuir*. 2016;32(16):3995–4003. doi:10.1021/acs.langmuir.5b04496
12. Zhang Z, Wang J, Chen C. Near-infrared light-mediated nanoplatforms for cancer thermo-chemotherapy and optical imaging. *Adv Mater*. 2013;25(28):3869–3880. doi:10.1002/adma.201301890

13. Singh AV, Jahnke T, Wang S, et al. Anisotropic Gold Nanostructures: optimization via in Silico Modeling for Hyperthermia. *ACS Applied Nano Materials*. 2018;1(11):6205–6216. doi:10.1021/acsanm.8b01406
14. Singh AV, Alapan Y, Jahnke T, et al. Seed-mediated synthesis of plasmonic gold nanoribbons using cancer cells for hyperthermia applications. *J Mater Chem B*. 2018;6(46):7573–7581. doi:10.1039/c8tb02239a
15. Singh AV, Jungnickel H, Leibrock L, et al. ToF-SIMS 3D imaging unveils important insights on the cellular microenvironment during biomineralization of gold nanostructures. *Sci Rep*. 2020;10(1):261. doi:10.1038/s41598-019-57136-w
16. Shin SH, Bode AM, Dong Z. Precision medicine: the foundation of future cancer therapeutics. *NPJ Precis Oncol*. 2017;1(1):12. doi:10.1038/s41698-017-0016-z
17. Singh AV, Dad Ansari MH, Dayan CB, et al. Multifunctional magnetic hairbot for untethered osteogenesis, ultrasound contrast imaging and drug delivery. *Biomaterials*. 2019;219:119394. doi:10.1016/j.biomaterials.2019.119394
18. Yu S, Cheng B, Yao T, et al. New generation ICG-based contrast agents for ultrasound-switchable fluorescence imaging. *Sci Rep*. 2016;6:35942. doi:10.1038/srep35942
19. Shang T, Yu X, Han S, et al. Nanomedicine-based tumor photothermal therapy synergized immunotherapy. *Biomater Sci*. 2020;8(19):5241–5259. doi:10.1039/d0bm01158d
20. Fan Z, Liu H, Xue Y, et al. Reversing cold tumors to hot: an immunoadjuvant-functionalized metal-organic framework for multimodal imaging-guided synergistic photo-immunotherapy. *Bioact Mater*. 2021;6(2):312–325. doi:10.1016/j.bioactmat.2020.08.005
21. Jo G, Lee BY, Kim EJ, et al. Indocyanine Green and Methyl-beta-Cyclodextrin Complex for Enhanced Photothermal Cancer Therapy. *Biomedicines*. 2020;8(11):476. doi:10.3390/biomedicines8110476
22. Yu Y, Zhang Z, Wang Y, et al. A new NIR-triggered doxorubicin and photosensitizer indocyanine green co-delivery system for enhanced multidrug resistant cancer treatment through simultaneous chemo/photothermal/photodynamic therapy. *Acta Biomater*. 2017;59:170–180. doi:10.1016/j.actbio.2017.06.026
23. Liebel F, Kaur S, Ruvolo E, et al. Irradiation of skin with visible light induces reactive oxygen species and matrix-degrading enzymes. *J Invest Dermatol*. 2012;132(7):1901–1907. doi:10.1038/jid.2011.476
24. Cohen L, Brodsky MA, Zubair R, et al. Cutaneous Interaction with Visible Light: what Do We Know. *J Am Acad Dermatol*. 2020;11(4):S0190. doi:10.1016/j.jaad.2020.03.115
25. Han HS, Choi KY. Advances in Nanomaterial-Mediated Photothermal Cancer Therapies: toward Clinical Applications. *Biomedicines*. 2021;9(3):305. doi:10.3390/biomedicines9030305
26. Yang W, Qiu W, Georgitzikis E, et al. Mitigating Dark Current for High-Performance Near-Infrared Organic Photodiodes via Charge Blocking and Defect Passivation. *ACS Appl Mater Interfaces*. 2021;13(14):16766–16774. doi:10.1021/acsami.1c02080
27. Ren Y, Sedgwick AC, Chen J, et al. Manganese(II) Texaphyrin: a Paramagnetic Photoacoustic Contrast Agent Activated by Near-IR Light. *J Am Chem Soc*. 2020;142(38):16156–16160. doi:10.1021/jacs.0c04387
28. Saneja A, Kumar R, Arora D, et al. Recent advances in near-infrared light-responsive nanocarriers for cancer therapy. *Drug Discov Today*. 2018;23(5):1115–1125. doi:10.1016/j.drudis.2018.02.005
29. Zhang F, Wu Q, Liu H. NIR light-triggered nanomaterials-based prodrug activation towards cancer therapy. *Wiley Interdiscip Rev Nanomed Nanobiotechnol*. 2020;12(6):e1643. doi:10.1002/wnan.1643
30. Wang H, Li X, Tse B, et al. Indocyanine green-incorporating nanoparticles for cancer theranostics. *Theranostics*. 2018;8(5):1227–1242. doi:10.7150/thno.22872
31. Abu-Rustum NR, Angioli R, Bailey AE, et al. IGCS Intraoperative Technology Taskforce. Update on near infrared imaging technology: beyond white light and the naked eye, indocyanine green and near infrared technology in the treatment of gynecologic cancers. *Int J Gynecol Cancer*. 2020;30(5):670–683. doi:10.1136/ijgc-2019-001127
32. Egloff-Juras C, Bezdetnaya L, Dolivet G, et al. NIR fluorescence-guided tumor surgery: new strategies for the use of indocyanine green. *Int J Nanomedicine*. 2019;14:7823–7838. doi:10.2147/IJN.S207486
33. Hu H, Qi Q, Dong Z, et al. Albumin coated trimethyl chitosan-based targeting delivery platform for photothermal/chemo-synergistic cancer therapy. *Carbohydr Polym*. 2020;241:116335. doi:10.1016/j.carbpol.2020.116335
34. Ma H, Yang X, Ke J, et al. Smart Assembled Human Serum Albumin Nanocarrier Enhanced Breast Cancer Treatment and Antitumor Immunity by Chemo- photothermal Therapy. *ACS Biomater Sci Eng*. 2020;6(5):3217–3229. doi:10.1021/acsbiomaterials.0c00286
35. Zhang W, Xia L, Ren X, et al. The improved targeting of an aspirin prodrug albumin-based nanosystem for visualizing and inhibiting lung metastasis of breast cancer. *Biomater Sci*. 2020;8(21):5941–5954. doi:10.1039/d0bm01035a
36. Colby AH, Oberlies NH, Pearce CJ, Herrera VLM, Colson YL, Grinstaff MW. Nanoparticle drug-delivery systems for peritoneal cancers: a case study of the design, characterization and development of the expansile nanoparticle. *Wiley Interdiscip Rev Nanomed Nanobiotechnol*. 2017;9(3). doi:10.1002/wnan.1451
37. Fang J, Wang Q, Yang G, et al. Albumin-MnO gated hollow mesoporous silica nanosystem for modulating tumor hypoxia and synergetic therapy of cervical carcinoma. *Colloids Surf B Biointerfaces*. 2019;179:250–259. doi:10.1016/j.colsurfb.2019.03.070
38. Huang Y, Hu L, Huang S, et al. Curcumin-loaded galactosylated BSA nanoparticles as targeted drug delivery carriers inhibit hepatocellular carcinoma cell proliferation and migration. *Int J Nanomed*. 2018;13::8309–8323. doi:10.2147/IJN.S184379
39. An F, Yang Z, Zheng M, et al. Rationally assembled albumin/indocyanine green nanocomplex for enhanced tumor imaging to guide photothermal therapy. *J Nanobiotechnology*. 2020;18(1):49. doi:10.1186/s12951-020-00603-8
40. Singh AV, Maharjan RS, Kanase A, et al. Machine-Learning-Based Approach to Decode the Influence of Nanomaterial Properties on Their Interaction with Cells. *ACS Appl Mater Interfaces*. 2021;13(1):1943–1955. doi:10.1021/acsami.0c18470
41. Wang J, Zhang C. CuGeO Nanoparticles: an Efficient Photothermal Theragnosis Agent for CT Imaging-Guided Photothermal Therapy of Cancers. *Front Bioeng Biotechnol*. 2020;8:590518. doi:10.3389/fbioe.2020.590518
42. Mazrad Z, Phuong P, Choi C, et al. pH/Redox-Triggered Photothermal Treatment for Cancer Therapy Based on a Dual-Responsive Cationic Polymer Dot. *ChemMedChem*. 2018;13(22):2437–2447. doi:10.1002/cmdc.201800538
43. Hu Q, Wang K, Qiu L. 6-Aminocaproic acid as a linker to improve near-infrared fluorescence imaging and photothermal cancer therapy of PEGylated indocyanine green. *Colloids Surf B Biointerfaces*. 2021;197:111372. doi:10.1016/j.colsurfb.2020
44. Shi Z, Chu C, Zhang Y, et al. Self-Assembled Metal-Organic Nanoparticles for Multimodal Imaging-Guided Photothermal Therapy of Hepatocellular Carcinoma. *J Biomed Nanotechnol*. 2018;14(11):1934–1943. doi:10.1166/jbn.2018.2636
45. Lin Z, Xi L, Chen S, et al. Uptake and trafficking of different sized PLGA nanoparticles by dendritic cells in imiquimod-induced psoriasis-like mice model. *Acta Pharm Sin B*. 2021;11(4):1047–1055. doi:10.1016/j.apsb.2020.11.008
46. Xu L, Wang SB, Xu C, et al. Multifunctional Albumin-Based Delivery System Generated by Programmed Assembly for Tumor-Targeted Multimodal Therapy and Imaging. *ACS Appl Mater Interfaces*. 2019;11(42):38385–38394. doi:10.1021/acsami.9b11263
47. Singh AV, Chandrasekar V, Janapareddy P, et al. Emerging Application of Nanorobotics and Artificial Intelligence To Cross the BBB: advances in Design, Controlled Maneuvering, and Targeting of the Barriers. *ACS Chem Neurosci*. 2021;12(11):1835–1853. doi:10.1021/acschemneuro.1c00087

48. Dwivedi C, Pandey H, Pandey AC, et al. In Vivo Biocompatibility of Electrospun Biodegradable Dual Carrier (Antibiotic + Growth Factor) in a Mouse Model-Implications for Rapid Wound Healing. *Pharmaceutics*. 2019;11(4):180. doi:10.3390/pharmaceutics11040180
49. Qiu T, Lan Y, Wei Z, et al. In vivo Multi-scale Photoacoustic Imaging Guided Photothermal Therapy of Cervical Cancer based on Customized Laser System and Targeted Nanoparticles. *Int J Nanomedicine*. 2021;16:2879–2896. doi:10.2147/ijn.S301664
50. Chen Y, Zhang L, Li F, et al. Combination of Chemotherapy and Photodynamic Therapy with Oxygen Self-Supply in the Form of Mutual Assistance for Cancer Therapy. *Int J Nanomedicine*. 2021;16:3679–3694. doi:10.2147/IJN.S298146
51. Liu X, Wang C, Ma H, et al. Water-Responsive Hybrid Nanoparticles Codelivering ICG and DOX Effectively Treat Breast Cancer via Hyperthermia-aided DOX Functionality and Drug Penetration. *Adv Healthc Mater*. 2019;8(8):e1801486. doi:10.1002/adhm.201801486
52. Wang J, Wu X, Shen P, et al. Applications of Inorganic Nanomaterials in Photothermal Therapy Based on Combinational Cancer Treatment. *Int J Nanomedicine*. 2020;15:1903–1914. doi:10.2147/ijn.S298146